Draft version November 6, 2019
Typeset using LaTeX default style in AASTeX63

Supplementary Information

1. BULK FORCING OF INTERNAL GRAVITY WAVES

We use the non-adiabatic g-mode oscillations of a star as a basis to expand velocity perturbations. For a given spherical harmonic degree ℓ, we have

$$\boldsymbol{u}_\ell(r,t) = \sum_{\omega'} A_\ell(t;\omega')\tilde{\boldsymbol{u}}_\ell(r;\omega')\exp(-i\omega' t), \tag{1}$$

where $\tilde{\boldsymbol{u}}_\ell$ corresponds to the velocity eigenfunction, and ω' its (complex) frequency. For simplicity of notation, here we will write frequencies in terms of the angular frequency $\omega = 2\pi f$, and write velocity perturbations as $\boldsymbol{u}$, instead of $\delta\boldsymbol{u}$ as in the main text. The velocity eigenfunctions are related to the displacement eigenfunctions via $\tilde{\boldsymbol{u}}_\ell = -i\omega'\tilde{\boldsymbol{\xi}}_\ell$. All vectors are assumed to be composed of two components: a radial component, e.g., u_r; and a horizontal component which is assumed to be proportional to the horizontal gradient of a spherical harmonic function, e.g., $\boldsymbol{u}_h = u_h\boldsymbol{\nabla}_h Y_{\ell,m}(\theta,\phi)$, where $\boldsymbol{\nabla}_h$ represents a horizontal angular derivative.

The eigenfunctions satisfy

$$-i\omega'\tilde{\boldsymbol{u}}_\ell = \mathcal{L}(\tilde{\boldsymbol{u}}_\ell), \tag{2}$$

where $\mathcal{L}$ is the linear wave operator. We define the dual basis $\tilde{\boldsymbol{u}}_\ell^\dagger$ by

$$\langle\tilde{\boldsymbol{u}}_\ell^\dagger(\omega'),\tilde{\boldsymbol{u}}_\ell(\omega'')\rangle = \delta_{\omega',\omega''}, \tag{3}$$

where δ is the Kronecker delta function, and the inner product is defined as

$$\langle\boldsymbol{f},\boldsymbol{g}\rangle \equiv \int_0^{R_\star} 4\pi\rho r^2\boldsymbol{f}^*\cdot\boldsymbol{g}dr. \tag{4}$$

We can define the dual basis in this way because the eigenvalues are non-degenerate. The set of all adiabatic modes are a complete basis (e.g., Eisenfeld 1969). Non-adiabatic modes are likely not complete (personally communication, R. H. D. Townsend 2019). Nevertheless, we expect they can represent almost all functions in the regions of the star which do not experience strong damping. The good agreement with calculations using Dedalus indicates the non-adiabatic modes can faithfully represent traveling waves.

We now introduce a forcing to the system,

$$\partial_t\boldsymbol{u}_\ell(r,t) = \mathcal{L}(\boldsymbol{u}_\ell) + \boldsymbol{f}_\ell(r,t;\omega). \tag{5}$$

The forcing has magnitude $F_{\omega,\ell}$, is assumed to act in only the horizontal directions, at the forcing radius r_f, and at frequency ω,

$$\boldsymbol{f}_\ell(t;\omega) = F_{\omega,\ell}\,\delta(r-r_f)\exp(-i\omega t)\boldsymbol{\nabla}_h Y_{\ell,m}(\theta,\phi), \tag{6}$$

where δ is the Dirac delta function. We can solve equation 5 by using the expansion in normal modes (equation 1) and projecting out with $\tilde{\boldsymbol{u}}_\ell^\dagger(\omega)$. This gives

$$[-i\omega' A_\ell(t;\omega') + \partial_t A_\ell(t;\omega')]\exp(-i\omega' t) = -i\omega' A_\ell(t;\omega')\exp(-i\omega' t) + \langle\tilde{\boldsymbol{u}}_\ell^\dagger(\omega'),\boldsymbol{f}(\omega)\rangle. \tag{7}$$

Defining $\tilde{\boldsymbol{u}}_h^\dagger = \tilde{u}_h^\dagger\boldsymbol{\nabla}_h Y_{\ell,m}(\theta,\phi)$ and assuming ρ is a function of radius, we can simplify this to

$$\partial_t A_\ell(t;\omega') = 4\pi\rho(r_f)r_f^2\tilde{u}_h^\dagger(r_f;\omega')\ell(\ell+1)F_{\omega,\ell}\exp\left[-i\left(\omega-\omega'\right)t\right]. \tag{8}$$

This can be solved together with the boundary condition $A_\ell = 0$ at $t = 0$,

$$A_\ell(t;\omega') = i4\pi\rho(r_f)r_f^2\tilde{u}_h^\dagger(r_f;\omega')\ell(\ell+1)F_{\omega,\ell}\frac{\exp\left[-i\left(\omega-\omega'\right)t\right]-1}{\omega-\omega'}. \tag{9}$$

Substituting this into equation 1, we find

$$\boldsymbol{u}_\ell(r,t) = 4\pi\rho(r_f)r_f^2\ell(\ell+1)F_{\omega,\ell}\left[\sum_{\omega'} i\tilde{u}_h^\dagger(r_f;\omega')\tilde{\boldsymbol{u}}_\ell(r;\omega')\frac{\exp(-i\omega t)-\exp(-i\omega' t)}{\omega-\omega'}\right]. \tag{10}$$

If all the eigenmodes are damped, the imaginary part of ω' is negative. As $t \to \infty$, the second exponential term drops out, and we find

$$\boldsymbol{u}_\ell(r,t) = 4\pi\rho(r_f)r_f^2\ell(\ell+1)F_{\omega,\ell}\left[\sum_{\omega'}\frac{i\tilde{u}_h^\dagger(r_f;\omega')\tilde{\boldsymbol{u}}_\ell(r;\omega')}{\omega-\omega'}\right]\exp(-i\omega t). \tag{11}$$

The surface luminosity fluctuations are then

$$\delta L_\ell(R_\star,t) = 4\pi\rho(r_f)r_f^2\ell(\ell+1)F_{\omega,\ell}\left[\sum_{\omega'}\frac{i\tilde{u}_h^\dagger(r_f;\omega')\delta\tilde{L}_\ell(R_\star;\omega')}{\omega-\omega'}\right]\exp(-i\omega t), \tag{12}$$

where $\delta\tilde{L}_\ell(R_\star;\omega')$ is the surface luminosity perturbation of the mode with frequency ω'. In practice, for many stellar models, we find that all modes calculated using GYRE are damped. Some stellar models do have some unstable modes with small positive growth rates. Nevertheless, we treat the time dependence of these modes in the same way as damped modes.

2. CONNECTION BETWEEN BULK FORCING AND INTERFACE FORCING

Theories (e.g., Lecoanet & Quataert 2013) and simulations (e.g., Rogers et al. 2013) make predictions for how the radial velocity perturbations at the radiative-convective boundary depends on frequency and spherical harmonic degree, $u_r(r_{\rm RCB};\omega,\ell)$. To use equation 12, we need to establish a link between the radial velocity perturbations and the forcing amplitude $F_{\omega,\ell}$.

To illustrate this connection, we will solve the bulk and interfacing forcing problems for an inviscid, adiabatic, Boussinesq fluid in Cartesian geometry. We assume the background has a constant Brunt-Väisälä frequency, N, ranges from $z = 0$ to L, that gravity is in the z direction, and that the perturbations are periodic in the horizontal directions. For impenetrable boundary conditions ($u_z(0) = u_z(L) = 0$), the eigenmodes are

$$u_z(z;k_h) = \sin(k_z z), \tag{13}$$

where

$$k_z^2(\omega) = k_h^2\left(\frac{N^2}{\omega^2}-1\right). \tag{14}$$

The horizontal wavenumber k_h is defined by $-k_h^2 u_z = \nabla_h^2 u_z$. The eigenvalues are frequencies ω which satisfy $k_z L = n\pi$, for an integer n.

Now consider the problem with boundary forcing. Our new boundary conditions are $u_z(0) = F_B\sin(\omega t)$, and $u_z(L) = 0$. The solution to this new problem is

$$u_z = F_B\left[\cos(k_z z) - \frac{\cos(k_z L)}{\sin(k_z L)}\sin(k_z z)\right]\sin(\omega t). \tag{15}$$

Recall that k_z is a function of the forcing frequency (equation 14). One can verify that this satisfies the boundary conditions. We can calculate the amplitude of u_z using

$$\left(\frac{1}{L}\int_0^L u_z^2 dz\right)^{1/2} = \sqrt{\frac{1}{2}}\frac{F_B}{|\sin(k_z L)|} + \mathcal{O}\left((k_z L)^{-1/2}\right). \tag{16}$$

The amplitude diverges when $k_z L = n\pi$, for n an integer. This corresponds to the frequencies of the eigenmodes of the system with impenetrable boundary conditions. Thus, the solution to the forced problem is related to the unforced eigenvalue problem, even though they have different boundary conditions. Because the problem has no dissipation, the amplitude divergences when forced at an eigenfrequency; if thermal dissipation is included, the divergence is regularized as the eigenfrequencies become complex.

Next consider the bulk forcing problem. Here we solve the problem with impenetrable boundary conditions, but including a forcing term to the horizontal velocity equation, similar to equation 5,

$$\partial_t \boldsymbol{u}_h + \boldsymbol{\nabla}_h p = F_{\omega,k_h}\delta(z - z_f)\cos(\omega t)\boldsymbol{\nabla}_h g(\boldsymbol{x}_h), \tag{17}$$

where $g(\boldsymbol{x}_h)$ satisfies $\nabla_h^2 g = -k_h^2 g$. Away from z_f, u_z is sinusoidal with wavenumber k_z. There are two additional conditions on u_z at $z = z_f$. The first is that $\partial_z u_z$ is continuous, and the second is

$$\partial_t \Delta u_z = k_h^2 F_{\omega,k_h}\cos(\omega t) g(\boldsymbol{x}_h), \tag{18}$$

where $\Delta u_z = u_z(z_f + \epsilon) - u_z(z_f - \epsilon)$, in the limit that $\epsilon \to 0$. The solution is

$$u_z = \begin{cases} -\frac{k_h^2}{\omega} F_{\omega,k_h}\left[\cos(k_z z_f)\frac{\cos(k_z L)}{\sin(k_z L)} + \sin(k_z z_f)\right]\sin(k_z z)\sin(\omega t) & z < z_f \\ -\frac{k_h^2}{\omega} F_{\omega,k_h}\frac{\cos(k_z z_f)}{\sin(k_z L)}\sin(k_z(z-L))\sin(\omega t) & z > z_f \end{cases} \tag{19}$$

where for simplicity we have dropped the horizontal dependence. Averaging over the region above z_f, we find

$$\left(\frac{1}{L - z_f}\int_{z_f}^{L} u_z^2 dz\right)^{1/2} \equiv \overline{u}_z(z_f) = \sqrt{\frac{1}{2}}\frac{k_h^2}{\omega}F_{\omega,k_h}\frac{|\cos(k_z z_f)|}{|\sin(k_z L)|} + \mathcal{O}\left((k_z L)^{-1/2}\right). \tag{20}$$

As in the boundary-forced problem, we find a divergence in the response when $k_z L = n\pi$, for n an integer (assuming $\cos(k_z z_f)$ is not also zero). If we also average $\overline{u}_z$ over a range Δz of z_f, we find

$$\frac{1}{\Delta z}\int_{z_0}^{z_0+\Delta z}\overline{u}_z(z_f)dz_f = \frac{\sqrt{2}}{\pi}\frac{k_h^2}{\omega}F_{\omega,k_h}\frac{1}{|\sin(k_z L)|} + \mathcal{O}\left((k_z\Delta z)^{-1/2}\right), \tag{21}$$

provided $k_z \Delta z \gg 1$.

Thus, if we average over a sufficiently large range of forcing locations, we find the boundary-forced and bulk-forced responses are equivalent, with the identification

$$F_{\omega,k_h} = \frac{\pi}{2}\frac{\omega}{k_h^2}F_B. \tag{22}$$

One can perform similar calculations including the results of thermal diffusivity (not shown here), and find the same relation between the boundary-forced and bulk-forced responses. We hypothesize that this relation is universal, and also carries over to the more realistic calculations with density variation, spherical geometry, etc. Then we have the following equation,

$$F_{\omega,\ell} = \frac{\pi}{2}\frac{\omega r_f}{\ell(\ell+1)}u_r(r_{\mathrm{RCB}};\omega,\ell). \tag{23}$$

Substituting into equation 12, we find

$$\delta L_\ell(R_\star,t) = u_r(r_{\mathrm{RCB}};\omega,\ell)\left(2\pi^2\rho(r_f)r_f^3\omega\right)\left[\sum_{\omega'}\frac{i\tilde{u}_h^\dagger(r_f;\omega')\delta\tilde{L}_\ell(R_\star;\omega')}{\omega-\omega'}\right]\exp(-i\omega t). \tag{24}$$

Finally, we have that the transfer function $T(f) \equiv T(\omega/2\pi)$, defined in equation 1 of the main text, is given by

$$T(\omega) = \frac{1}{\Delta r}\int_{r_0}^{r_0+\Delta r} 2\pi^2\rho(r_f)r_f^3\omega\left[\sum_{\omega'}\frac{i\tilde{u}_h^\dagger(r_f;\omega')\delta\tilde{L}_\ell(R_\star;\omega')}{\omega-\omega'}\right]dr_f. \tag{25}$$

3. STELLAR STRUCTURE MODELS

We calculate the transfer function for twelve stellar structure models generated by MESA (Paxton et al. 2011, 2013, 2015, 2018, 2019). We use models with ZAMS masses of $3M_\odot$, $7M_\odot$, $10M_\odot$, and $20M_\odot$, at three different evolutionary stages during the main sequence: when their core H fraction is about 0.66 (near the ZAMS), 0.33, and 0.01 (TAMS). Models were calculated assuming a metallicity $Z = 0.02$. Convective boundaries were determined using the Schwarzschild criterion, with convective velocities calculated using the mixing length theory in the Henyey formulation with $\alpha_{\rm MLT} = 1.6$. Above the convective core, a step overshooting with $\alpha_{\rm ov} = 0.29$ was included. The models were computed using gold tolerances and the *dedt*-form of the energy equation, which provides superior results for energy conservation (Paxton et al. 2019). Details of the calculations, including a typical `inlist`, can be found at https://github.com/matteocantiello/gyre_igw.

4. BULK FORCING CALCULATIONS WITH GYRE

We use GYRE (Townsend et al. 2018) to calculate non-adiabatic normal modes for each stellar model. We use a second-order Gauss-Legendre collocation scheme, which we found to give more robust eigenfunctions than higher-order schemes. The grid is calculated using `n_inner=5`, `alpha_osc=20`, and `alpha_exp=4`. Increasing the grid resolution did not change the transfer function at high frequencies, but leads to more numerical noise at very low frequencies. We search for modes using the `grid_type='INVERSE'` method, and pick the maximum frequency such that we find all of the highest frequency g-modes, and the minimum frequency such that we can resolve the fast decay of the transfer function for strongly damped modes. Although p-modes are important for the (near) completeness of the eigenmode basis, we find that they have a negligible contribution to the transfer function. This is because $\tilde{u}_h^\dagger(r_f)$ is small for p-modes, which are localized near the surface of the star, and there is poor frequency matching, so $\omega - \omega'$ is large. All GYRE inlists are at https://github.com/lecoanet/massive_star_igw.

Once we have the g-mode eigenmodes, we calculate the dual basis according to equation 3. We then calculate the surface luminosity perturbation for a single r_f. Although convection likely forces waves simultaneously over a range of radii, we use a delta-function forcing as we only study the propagation of the waves after they have been excited. To calculate the transfer function, we average over 50 equally-spaced values of r_f with $\Delta r = 0.02 R_\star$. All our stellar models have sharp composition gradients just outside the convection zone. We find that if we pick r_f below this composition gradient, the transfer function is dominated by numerical noise. Thus, we pick $r_0 = 0.25 R_\star$ for all models except the $20M_\odot$ model near the ZAMS, for which we pick $r_0 = 0.35 R_\star$. Increasing r_0 above these values changes the overall normalization of the transfer function—waves experience less amplification if they are generated at larger radii—but not the shape.

At the lowest frequencies, we sometimes find the transfer function abruptly changes slope. This stems from numerical errors in the eigenfunctions and/or eigenvalues. The exact position of this region changes with any change in numerical method (e.g., changing the grid resolution, number of modes, or r_0). We expect this region would not be present in more accurate calculations.

The transfer function becomes extremely large near the standing mode frequencies at high frequencies. To find these peaks, we initially calculate the transfer function for a grid of frequencies which are roughly equally spaced logarithmically. Then we recalculate the transfer function on a grid which is refined near the peaks. We recursively refine until the peaks of the transfer function are well-resolved. It is important to resolve the peaks of the transfer function to ensure we correct measure the frequency-integrated power in each peak.

5. INTERFACE FORCING CALCULATIONS USING DEDALUS

We now describe the solution of the forcing problem via numerical integration of the evolution equations using Dedalus. Here we force the waves with a bottom boundary condition, which is equivalent to the bulk forcing used in GYRE (section 2). There are two important reasons for performing these calculations using Dedalus. First, we can test the robustness of the GYRE calculation by comparing with a second calculation using a completely different method. Second, the Dedalus calculations make a different set of simplifying assumptions than the GYRE calculations, so we can test the sensitivity to assumptions made when using GYRE. The GYRE calculations assume the g-modes form a basis for the traveling wave calculation, and they also force waves at r_f, which is above the radiative-convective boundary. In contrast, our calculations with Dedalus expand perturbations in Chebyshev polynomials, which are known to form a complete basis, and we force the waves at the radiative-convective boundary. On the other hand, some short-comings of the Dedalus simulations include: 1. We solve the equations in the Cowling approximation;

2. Our simulations domain does not extent to $r = 0$ or $r = R_\star$, because if it include a convection zone, simulations become dominated by exponentially-growing convection modes; 3. Very long integrations are required to resolve the standing mode peaks; and, 4. The Dedalus calculations are much slower than the GYRE calculations.

We use Dedalus to solve the linearized evolution equations in the Cowling approximation,

$$\partial_t u_r + \partial_r p + p\frac{d\log\rho_0}{dr} + \frac{g_c\rho_c R_\star}{p_c} g_0\rho = 0, \tag{26}$$

$$\partial_t u_h + \frac{p}{r} = 0, \tag{27}$$

$$r^2\Upsilon - \partial_r(r^2 u_r) - \ell(\ell+1) r u_h = 0, \tag{28}$$

$$\partial_t\rho + u_r\frac{d\log\rho_0}{dr} + \Upsilon = 0, \tag{29}$$

$$\nu_T T - \left(\nu_T\nabla_{\rm ad} + \Gamma_1^{-1}\right)\frac{T_0\rho_0}{p_0}p + T_0\rho = 0, \tag{30}$$

$$L - L_0\left[\left(\frac{dT_0}{dr}\right)^{-1}\partial_r T + 3\frac{T}{T_0} - \rho\right] = 0, \tag{31}$$

$$\partial_t p + \frac{1}{\rho_0}\frac{dp_0}{dr}u_r + c_{s,0}^2\Upsilon + \frac{Cc_{s,0}^2\nu_T}{4\pi r^2\rho_0 T_0 c_p}\left(\partial_r L + L_0\frac{dT_0}{dr}\frac{\ell(\ell+1)}{r^2}T\right) = 0. \tag{32}$$

Here u_r is the radial velocity and u_h is the horizontal velocity given by $\boldsymbol{u}_h = u_h\boldsymbol{\nabla}_h Y_{\ell,m}(\theta,\phi)$, and Υ is the divergence of the velocity. The background density ρ_0, pressure p_0, gravitational acceleration g_0, temperature T_0, luminosity L_0, and specific heat at constant pressure c_p, are all taken from the MESA model, and are all normalized to their values at the bottom of the domain (at the radiative-convective interface). Their values at the bottom of the domain are denoted with subscript c. The thermodynamic quantities are defined as $\nu_T = -(\partial\log\rho/\partial\log T)_p$, $\nabla_{\rm ad} = (\partial\log T/\partial\log p)_s$, and $\Gamma_1 = (\partial\log p/\partial\log\rho)_s$, where s is the entropy. Radii are normalized to the stellar radius $R_\star$. p and ρ are the Eulerian pressure and density perturbation, both normalized to ρ_0. T and L are the Eulerian temperature and luminosity perturbations, normalized to T_c and L_c, respectively. The normalized adiabatic sound speed squared is $c_{s,0}^2 = \Gamma_1 p_0/\rho_0$. The constant C is given by

$$C = \frac{L_c}{T_c c_{p,c}\sqrt{p_c\rho_c}R_\star^2}. \tag{33}$$

We normalize time using

$$t_{\rm norm} = R_\star\sqrt{\frac{\rho_c}{p_c}}. \tag{34}$$

For boundary conditions, we use

$$u_r(r_{\rm bot}) = \sin(\omega t)\frac{1}{2}\left[1 + \tanh\left(\frac{t-t_0}{\Delta t}\right)\right], \tag{35}$$

$$u_r(r_{\rm top}) = s(r_{\rm bot}) = s(r_{\rm top}) = 0, \tag{36}$$

where $s = \rho - p/c_{s,0}^2$ is related to the entropy perturbation. We ramp up the boundary forcing starting at time $t_0 \approx 10P$ over a timescale $\Delta t \approx P$, where P is the wave period.

We discretize the problem by representing all background and perturbation variables in terms of Chebyshev series. We split up the domain into three segments. The first segment comprises r between $\approx 0.216R_\star$, the top of the convection zone, and $0.5R_\star$, and is represented using 512 Chebyshev modes. The second and third segments comprise r between $0.5R_\star$ and $0.8R_\star$, and between $0.8R_\star$ and $\approx 0.976R_\star$, which is just below the surface convection zone; both are represented using 256 Chebyshev modes. Boundary conditions impose continuity of all perturbation variables at the matching points, $0.5R_\star$ and $0.8R_\star$. Background quantities are expanded in Chebyshev polynomials, but coefficients less than 10^{-5} of the maximum coefficient in each segment are set to zero to make the problem sparser. For timestepping, we use a four stage, third-order accurate implicit-explicit Runge-Kutta timestepping scheme (Ascher et al. 1997), with

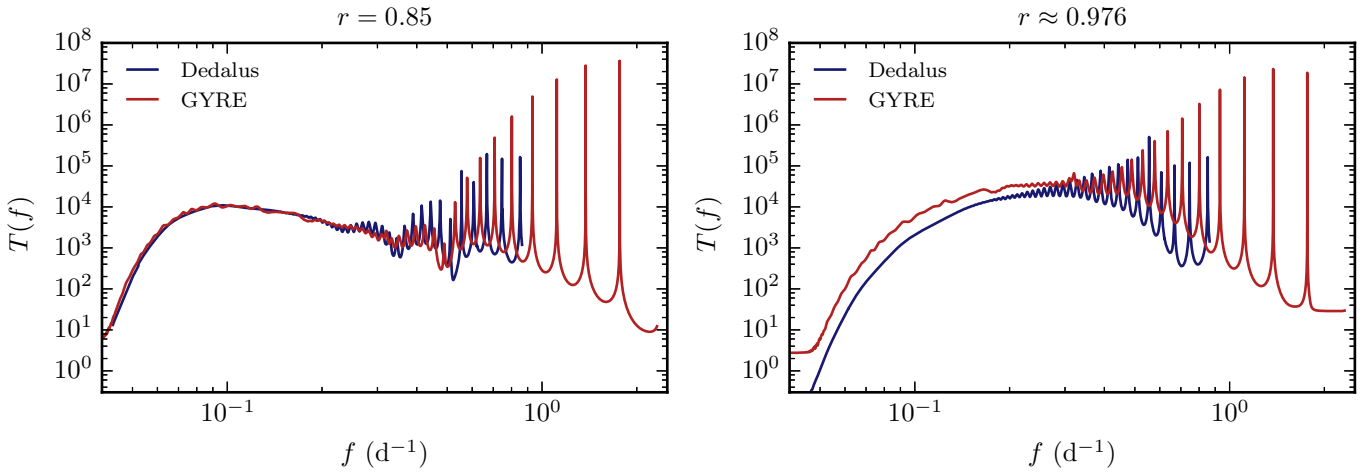

Figure 1. Comparison of the transfer function calculated in GYRE (red) and Dedalus (blue) for $\ell = 1$ motions for a $10M_\odot$ model near the ZAMS. In both panels, the Dedalus transfer functions are divided by 6. In the left (right) panel, we plot the transfer function where the luminosity is evaluated at $r = 0.85R_\star$ ($r \approx 0.976R_\star$). With the normalization factor of one sixth, there is excellent agreement at $r = 0.85R_\star$ between the two methods for low frequencies, and the two curves follow the same trends at higher frequencies. We believe the differences between the calculations at higher frequencies and also at $r \approx 0.976R_\star$ is due to different in boundary conditions between the two calculations.

timestep $\approx P/100$. We also ran simulations with double the spatial resolution and smaller timestep size, and found neither led to significant changes in the transfer function.

To calculate the transfer function, we wish to evolve the oscillation equations until they reach a statistically steady state. Unfortunately, this takes a very long time, especially when the forcing frequency is close to the oscillation frequency of one of the higher frequency standing modes. For low frequency modes, we evolve the system for $\approx 100P$, which long enough for the luminosity amplitude at the top boundary to saturate. For higher frequency waves, we evolve for $\approx 550P$. This integration time is sufficient, except for forcing frequencies very close to the oscillation frequencies of a standing mode. We have integrated as long as $\approx 10^4 P$ for some frequencies, but the luminosity at the top boundary still continues to grow with time. Thus, we can only provide lower limits on the transfer function near the four highest frequency standing waves. We also only calculate the transfer function up to $\approx 1\,\mathrm{d}^{-1}$. To calculate the transfer function, we calculate the root-mean-square luminosity perturbation at the top boundary (recall that the velocity perturbation at the bottom boundary has an amplitude of unity), over a portion of the integration time.

6. COMPARISON BETWEEN GYRE AND DEDALUS CALCULATIONS

Because the Dedalus calculations are more computationally expensive, we only calculated the transfer function for the $10M_\odot$ stellar model near the ZAMS. In figure 1 we compare our two methods for calculating the transfer function. We report the transfer function based off the luminosity in two locations: at $r = 0.85R_\star$, and also at $r \approx 0.976R_\star$ (at the top of the Dedalus simulations). Note that in GYRE, the transfer calculation evaluated at $r \approx 0.976R_\star$ is nearly identical to the transfer calculation evaluated at the surface.

The transfer functions measured with the two numerical techniques are very similar. At low frequencies, the transfer functions are very small, and there are regularly-spaced peaks at high frequencies.

However, the peaks are at different frequencies in the two codes. We believe this is due to differences in boundary conditions. At the surface, GYRE assumes no lagrangian pressure fluctuations, and a perturbed Stefan-Boltzmann equations; in Dedalus we set the radial velocity and eulerian entropy perturbation to zero at $r \approx 0.976R_\star$. At the inner boundary, GYRE includes a convection zone whereas the Dedalus domain does not. We do not expect the standing modes of the two problems to be the same, so the peaks in the transfer function should be at different frequencies. Note that there is always a Dedalus peak between every pair of GYRE peaks; this suggests that the period-spacing between the modes in the two calculations is very similar. Also recall that the amplitude of the four highest-frequence peaks in Dedalus are lower bounds on the transfer function, as we were not able to integrate long enough to establish the height of the peak. For this reason, we also did not calculate the transfer function in Dedalus for frequencies greater than $\approx 1\,\mathrm{d}^{-1}$.

The two calculations' transfer functions also have different amplitudes. In both panels of figure 1, we divided the Dedalus transfer function by six. With this normalization, we find excellent agreement between the amplitudes of the two signals at $r = 0.85R_\star$. We expect the Dedalus transfer function to be larger because the waves in Dedalus are excited at $r \approx 0.216R_\star$, whereas in GYRE we excited waves between $r = 0.25R_\star$ and $r = 0.27R_\star$. However, the waves only amplify by a factor of ≈ 2 between these points. Future work should examine the remaining difference in normalization between the calculations. In this work, we do not use the transfer function in any way that depends on its overall normalization.

We believe the difference between the normalization of the transfer functions calculated at $r \approx 0.976R_\star$ is also due to differences in outer boundary conditions. It appears that the choice of boundary condition in Dedalus leads to luminosity fluctuations which are smaller by a factor of ≈ 3 at the upper boundary than the choice used in GYRE. We find that the eigenfunctions in both codes match very well until they reach the surface. This explains the agreement at $r = 0.85R_\star$.

Although there are some differences between the GYRE and Dedalus calculations, we find them to be minor. In fact, it may even be surprising that the agreement is so good, given the completely different numerical methods and the various inconsistent assumptions made in the two calculations. This good agreement gives us confidence in the main features of the transfer function: the transfer function is small at low frequencies due to damping, and is characterized by regularly-spaced peaks due to standing modes at high frequencies.

7. TRANSFER FUNCTIONS FOR STARS OF DIFFERENT MASSES AND EVOLUTIONARY STAGES

In figure 2, we plot the transfer function, calculated using GYRE, for a range of stellar models of different ages and initial masses. We only plot the transfer function for $\ell = 1$ so it is easier to identify the trends with mass and age. The $\ell = 1$ modes are expected to dominate the disk-averaged luminosity variation, as higher ℓ modes have significant cancellation. The three ages we include correspond to core hydrogen fractions of 0.66 (near the ZAMS), 0.33 (labelled "mid"), and nearly zero (TAMS). In all cases, we find a smooth transfer function corresponding to traveling waves at low frequencies. These waves are strongly damped, so the transfer function is small. At higher frequencies, the transfer function is dominated by regularly-spaced peaks corresponding to standing modes.

More massive stars have fewer standing-mode peaks. This is because the luminosity of these stars is larger, so radiative damping is more important. Thus, damped traveling waves exist at higher frequencies for higher mass stars. Nevertheless, there are always several weakly damping standing modes, at least up to $20M_\odot$. Lower mass stars have an extremely large number of weakly damped standing modes. It is likely that $\approx 100\,\mathrm{d}$ TESS or K2 observations of $3M_\odot$ stars would not be able to resolve most the individual standing mode peaks. However, lower mass stars also have a larger Brunt-Väisälä frequency, so g-modes extend to higher frequency. We thus believe that standing modes peaks with frequencies $\sim 4 - 5\,d^{-1}$ should be detectable in observations of $\approx 3M_\odot$ stars, if such waves were efficiently excited by convection.

There are only minor changes in the transfer function as the stars evolve from the ZAMS to mid-way between ZAMS and TAMS. The frequencies of the highest modes increase modestly, and radiative damping becomes somewhat weaker, leading to more standing modes. However, we find substantial changes when the stars reach TAMS. Radiative damping becomes significantly weaker at TAMS, leading to many more standing modes. The frequency-spacing between the modes also seems smaller. Thus, it may be more difficult to detect individual standing modes for stars at the TAMS.

Several of our transfer functions have an abrupt change of slope at $\approx 0.05\,\mathrm{d}^{-1}$, e.g., ZAMS stars $\geq 7M_\odot$. This is a numerical effect; this feature changes magnitude and frequency range when we change the resolution of the modes, the number of modes used, etc. The Dedalus calculation shows the transfer function decreases smoothly past these frequencies (see figure 1, left panel). We believe the uptick in the transfer function for our $7M_\odot$ TAMS model at the lowest frequencies is also due to this type of numerical error. For our $3M_\odot$ TAMS model, we were not able to calculate the transfer function at low frequencies due to repeated floating-point exception errors thrown by GYRE.

At high frequencies, the transfer functions are dominated by very sharp peaks corresponding to standing modes. For many stellar models, the transfer function between these peaks seems to be nearly constant. We do not understand this behavior, but note that it seems to be robust to changes in numerical parameters, e.g., the resolution of the modes, the number of modes used, etc. It is unlikely that the behavior of the transfer function between the peaks have any observational implications.

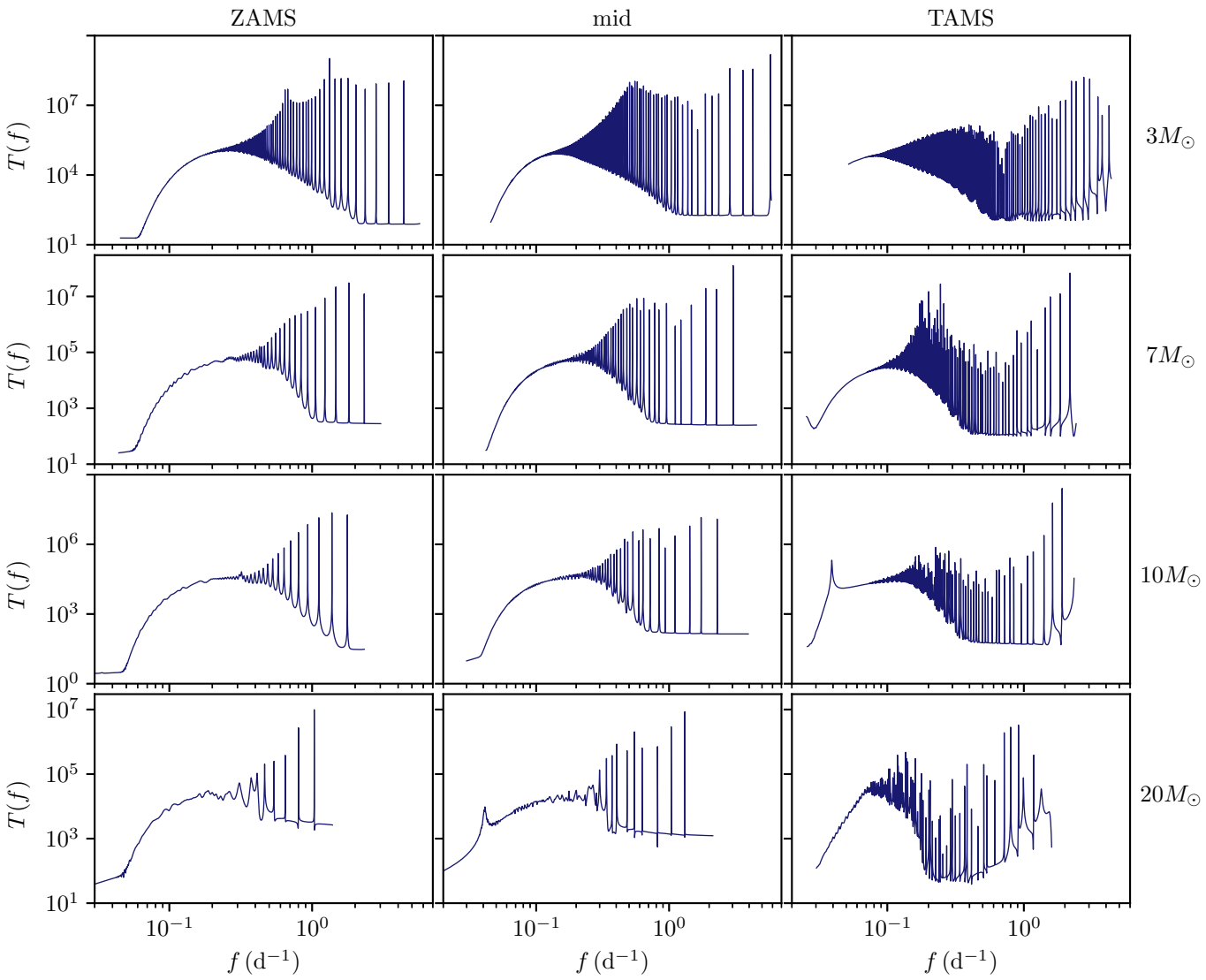

Figure 2. Transfer functions calculated in GYRE for $\ell = 1$ modes, for stellar models of different masses and ages. The three ages correspond to core hydrogen fractions of 0.66 (near the ZAMS), 0.33 (labelled "mid"), and nearly zero (TAMS). Less massive stars have less radiative damping, and thus have more standing modes than more massive stars. Radiative damping is also weaker at TAMS. However, all models show the same characteristic patterns: at low frequencies, the transfer function is smooth but small due to efficient wave damping, whereas at high frequencies, there are regularly-spaced peaks corresponding to standing modes.

Finally, we note that our $10M_\odot$ TAMS model and $20M_\odot$ "mid" model have well-defined peaks at $\approx 0.04\,\mathrm{d}^{-1}$. These appear to be numerically robust. We do not have a physical understanding of these features. If these features are physical, they may be detectable in long-duration observations of massive stars.

8. OVERALL SPECTRUM NORMALIZATION

Both LQ and R spectra have the normalization (Lecoanet & Quataert 2013; Rogers et al. 2013)

$$F_w \sim \mathcal{M} F_c, \tag{37}$$

where F_w is the total wave flux, and F_c is the convective flux. The efficiency of wave generation is given by $\mathcal{M}$, the convective Mach number, which we calculate using ω_c/N_0, where ω_c is the convective frequency, and N_0 is a typical value of the Brunt-Väisälä frequency in the radiative zone. The wave flux is dominated by waves near the convective frequency ω_c and $\Lambda H/r_{\mathrm{RCB}} \sim 1$, where r_{RCB} and H are the radius and the scaleheight at the radiative-convective

boundary, and $\Lambda = \sqrt{\ell(\ell+1)}$ as above. Thus, we have

$$\mathcal{M} F_c \sim \rho_{\rm RCB} H N_0 u_r^2, \tag{38}$$

where u_r is the radial velocity of waves with frequencies near ω_c and $\Lambda H / r_{\rm RCB} \sim 1$, and $\rho_{\rm RCB}$ is the density at the radiative convective boundary. We define $F_c = \rho_{\rm RCB} u_c^3$, and $\omega_c = u_c / H$. The we have

$$u_r \sim u_c \mathcal{M}. \tag{39}$$

Recall this estimate is only for the most energetic waves with frequencies near ω_c and $\Lambda H / r_{\rm RCB} \sim 1$.

We can now combine this with the predicted frequency and wavenumber scalings described in section 2 of the main text. The predictions for the radial velocity spectra are

$$u_r \sim u_c \mathcal{M} \left(\frac{\Lambda H}{r_{\rm RCB}} \right)^{-0.9} \left(\frac{f}{f_c} \right)^{0.4}, \qquad \text{(R spectrum)} \tag{40}$$

$$u_r \sim u_c \mathcal{M} \left(\frac{\Lambda H}{r_{\rm RCB}} \right)^{5/2} \left(\frac{f}{f_c} \right)^{-13/4}. \qquad \text{(LQ spectrum)} \tag{41}$$

To evaluate these expressions, we calculate the average convective velocity using

$$u_c^3 = \frac{\int_0^{r_{\rm RCB}} L_c dr}{\int_0^{r_{\rm RCB}} 4\pi r^2 \rho dr}, \tag{42}$$

where L_c is the convective luminosity. The convective *angular* frequency is $\omega_c = u_c / H$, and the convective frequency is $f_c = \omega_c / (2\pi)$. We use $N(r_{\rm RCB} + H) = N_0$ as our estimate of the Brunt-Väisälä frequency.

We calculate each of these terms using our $10 M_\odot$ MESA model near the ZAMS. We find $u_c \approx 0.01 R_\star/{\rm d}$, $\mathcal{M} \approx 0.002$, $r_{\rm RCB}/H \approx 2.3$, and $f_c \approx 0.018\,{\rm d}^{-1}$. Thus, the theoretical predictions for the radial velocities are

$$u_r \sim (2 \times 10^{-4}\, R_\star/{\rm d})\, \Lambda^{-0.9} f^{0.4}, \qquad \text{(R spectrum)} \tag{43}$$

$$u_r \sim (6 \times 10^{-12}\, R_\star/{\rm d})\, \Lambda^{5/2} f^{-13/4}. \qquad \text{(LQ spectrum)} \tag{44}$$

For comparison, in Figure 2 of the main text, we use a multiplying prefactor of $5 \times 10^{-8}\, R_\star/{\rm d}$ for the R spectrum, and $2 \times 10^{-11}\, R_\star/{\rm d}$ for the LQ spectrum. Thus, the R spectrum predicts surface variability many orders of magnitude higher than what is observed. It may seem that the LQ spectrum predicts a similar magnitude to the observed variability, even if the shape of the spectrum is very different. However, we believe this is likely coincidental, as the very steep frequency dependence of the LQ spectrum makes it difficult to predict the overall amplitude of the spectrum. For instance, if we had used a different definition of the convective frequency, leading to a change by 2π, the overall amplitude of the spectrum could be as low as 2×10^{-14} or as high as 3×10^{-9}. However, such a change in the definition of the convective frequency would lead to a very minor change in the R spectrum, because it has a very weak dependence on f_c. This illustrates the need to calibrate the spectrum and convective frequency from 3D simulations of core convection.

9. ROTATION

We have not included the effects of rotation in any of our calculations. Rotation plays an important role in the convective excitation of internal waves (Mathis et al. 2014). First, rotation can strongly constrain the convection, leading to flows which mostly align with the rotation axis (e.g., Augustson et al. 2016). This will modify the wave excitation process. Second, rotation changes the internal waves themselves. The eigenvalue problem for oscillation modes is one-dimensional without rotation, but becomes two-dimensional with rotation. This is because rotation couples together modes with different spherical harmonic degree ℓ, but does not couple modes with different azimuthal degree m. Oscillation modes with rotation can have non-trivial latitudinal structure.

Because of the two-dimensional nature of the oscillation problem with rotation, it is difficult to calculate the transfer function. However, we will comment on some expected properties of the transfer function with rotation. Internal waves cannot propagate at the poles for $f < 2/T_{\rm rot}$, where $T_{\rm rot}$ is the rotation period (not to be confused with the

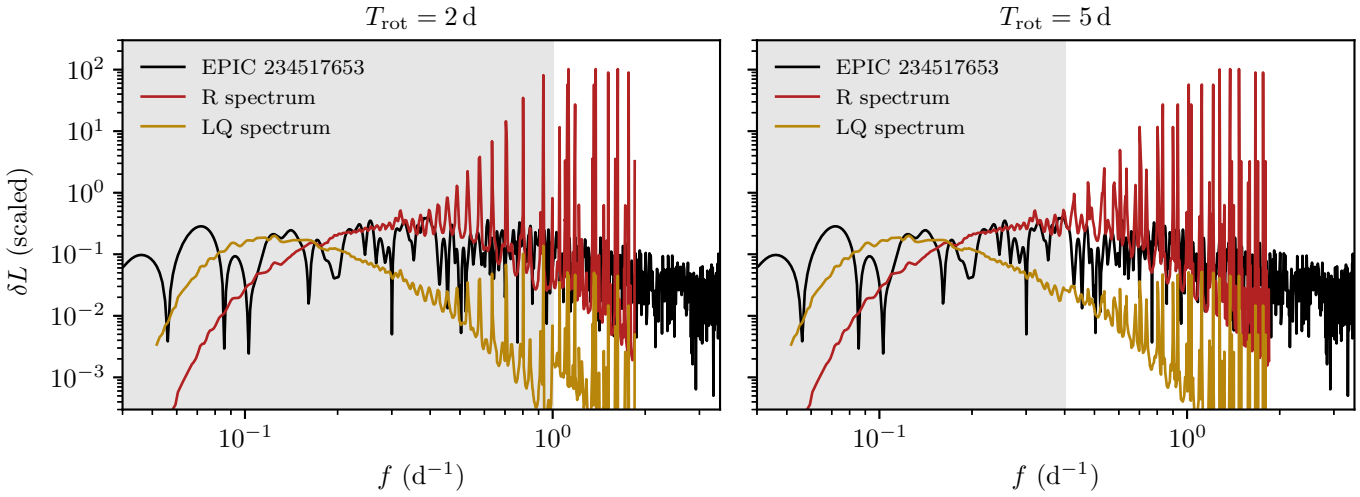

Figure 3. Luminosity variation spectrum for EPIC 234517653 from B19, and two rotationally-modified theoretical spectra, for two different rotation periods, $T_{\rm rot}$. For frequencies $f < 2/T_{\rm rot}$, shaded in grey, waves can only propagate near the equator, and there will be negligible luminosity variations for stars observed pole-on. For higher frequencies, rotation produces Doppler-shifts, leading to more peaks. Although there are more peaks, their frequency spacing is large enough to be resolved by the observations.

transfer function, T). The waves concentrate closer and closer to the equator in the limit that $fT_{\rm rot}/2$ goes to zero. These waves will cause negligible surface variability in stars observed from the poles. It is likely that at least some of the stars observed in B19 are observed nearly pole-on. These stars would show very little power at frequencies less than $2/T_{\rm rot}$ if the low-frequency variability was due to waves. However, a sharp decline in variability at low frequencies due to rotation is not observed in any of the stars, again suggesting that the variability is not due to waves.

If rotation is sufficiently weak (i.e., $f \gg 2/T_{\rm rot}$), then oscillation modes are Doppler-shifted by rotation, $f \rightarrow f + m/T_{\rm rot}$, where m is the azimuthal degree of the mode. If the convection is approximately isotropic, energy will be distributed between the different m modes evenly. Thus, each peak in the non-rotating transfer function will be evenly split into $2\ell + 1$ peaks under the influence of weak rotation. This will cause more peaks in the spectrum, and will change the spacing between peaks.

To illustrate these two effects, we plot rotationally-modified surface luminosity spectra in Figure 3. This requires choosing nominal rotation periods for massive stars. Dufton et al. (2013) and Ramírez-Agudelo et al. (2013) measured the rotation velocities of B & O type stars as part of the VLT-FLAMES Tarantula Survey. In both cases, they find rotation velocities around $100 - 300\,{\rm km/s}$. Assuming a typical radius of $10R_\odot$, these roughly correspond to rotation rates of $2 - 5\,{\rm d}$. This is in line with Nielsen et al. (2013), which reports a typical photometric rotation period for B stars of around $4\,{\rm d}$. With this in mind, we consider two possible rotation periods, $2\,{\rm d}$ and $5\,{\rm d}$, to demonstrate the possible effects of rotation. For frequencies less than $2/T_{\rm rot}$ (shaded in grey) we do not modify the spectrum. However, waves at these frequencies would be localized near the equator, and would have negligible surface manifestation for stars viewed pole-on. For frequencies greater than $2/T_{\rm rot}$, we split the power of each peak evenly into $2\ell+1$ peaks with frequencies $f + m/T_{\rm rot}$ for $|m| \leq \ell$, assuming the weak-rotation limit. This leads to more peaks at high frequencies, and a more complicated spectrum. However, most of the individual peaks should still be resolved by the observations, so the theoretical spectra still do not resemble the smooth observed spectra of B19.

REFERENCES

Ascher, U. M., Ruuth, S. J., & Spiteri, R. J. 1997, Appl. Numer. Math., 25, 151

Augustson, K. C., Brun, A. S., & Toomre, J. 2016, ApJ, 829, 92

Dufton, P. L., Langer, N., Dunstall, P. R., et al. 2013, A&A, 550, A109

Eisenfeld, J. 1969, Journal of the Institute of Mathematics and Its Applications, 26, 357

Lecoanet, D., & Quataert, E. 2013, MNRAS, 430, 2363

Mathis, S., Neiner, C., & Tran Minh, N. 2014, A&A, 565, A47

Nielsen, M. B., Gizon, L., Schunker, H., & Karoff, C. 2013, A&A, 557, L10

Paxton, B., Bildsten, L., Dotter, A., et al. 2011, ApJS, 192, 3

Paxton, B., Cantiello, M., Arras, P., et al. 2013, ApJS, 208, 4

Paxton, B., Marchant, P., Schwab, J., et al. 2015, ApJS, 220, 15

Paxton, B., Schwab, J., Bauer, E. B., et al. 2018, ApJS, 234, 34

Paxton, B., Smolec, R., Schwab, J., et al. 2019, ApJS, 243, 10

Ramírez-Agudelo, O. H., Simón-Díaz, S., Sana, H., et al. 2013, A&A, 560, A29

Rogers, T. M., Lin, D. N. C., McElwaine, J. N., & Lau, H. H. B. 2013, ApJ, 772, 21

Townsend, R. H. D., Goldstein, J., & Zweibel, E. G. 2018, MNRAS, 475, 879